

Cooperative emission from two coupled solid-state quantum emitters and its effect on random number generation

Madhura Ghosh Dastidar,¹ Aprameyan Desikan,² Gniewomir Sarbicki,³ and Vidya Praveen Bhallamudi¹

¹*Quantum Center of Excellence for Diamond and Emerging Materials (QuCenDiEM) Group,
Department of Physics, Indian Institute of Technology Madras, Chennai 600036, India*

²*Department of Physical Sciences, Indian Institute of Science Education &
Research Mohali Sector 81 SAS Nagar, Manauli PO 140306 Punjab, India*

³*Institute of Physics, Faculty of Physics, Astronomy and Informatics,
Nicolaus Copernicus University, Grudziądzka 5/7, 87-100 Toruń, Poland*

(Dated: August 20, 2024)

We discuss the behaviour of cooperative effects in the emitted light from a system of two nitrogen-vacancy (NV) centers confined in a nanopillar having dimensions close to the wavelength of the excitation pump. We experimentally observe a $g^{(2)}(0) > 0.5 \rightarrow 1$ for the coupled emitter system and a drastic decrease in the singlet and triplet lifetimes by a factor of ≈ 6 , indicating an interaction between the two emitters, which indicates superradiant behaviour. We theoretically study the dissipative dynamics of the interaction of the emitter system with the excitation light at a finite temperature for three cases (single emitter, two emitters with and without dipole-dipole coupling) by solving the Lindblad master equation and providing an analytical expression for the second-order correlation function. We observe that from the master equation, the populations and coherences mix for the two emitters' cases. Through this, we support our experimental results and discuss superradiance from our system. Finally, we discover a reliable quantum random number generation rate of ~ 200 kHz from the coupled emitter system, at low pump powers.

I. INTRODUCTION

The emerging field of quantum technologies has created a requirement for building single photon sources, useful for secure quantum key distribution [1] and quantum random number generation [2]. Further, random numbers are required for key generation in quantum cryptography. Generally, classical methods of producing random numbers produce pseudorandom numbers using algorithms [3]. However, the inherent randomness of a quantum system can be used to generate truly random numbers [4, 5]. This has been demonstrated in various ways [6–11], one of which involves single photon detection [2, 12–14]. When a stream of single photons is inputted to a symmetric beam-splitter, each photon gets randomly transmitted or reflected, randomness entropy is obtained from the "which-path" principle of the photon [15, 16].

Single photon sources should ideally be able to produce a stream of single photons on-demand [17]. On-demand single photon emission from several platforms such as quantum dots [18] and single molecules [19] have been tested but each has certain challenges [20]. Emitters such as single defects in solid-state systems have emerged as promising candidates for generating controllable and photostable single photon emitters, which can operate from cryogenic to room temperatures [21]. Among various solid-state emitters, negatively-charged nitrogen vacancy (NV) centers in diamond have shown a lot of potential in the development of scalable single photon sources due to their distinct optical [22–24] and spin [25, 26] properties which can be manipulated as their energy-level structure is known.

In general, as diamond has a high refractive index

of 2.41, the efficient extraction of single photons from NV centers embedded in bulk diamond is challenging. This problem can be overcome by embedding the NV centers in nanostructures constructed out of diamond, such as nanopillars [27–29], photonic crystals [30, 31] and whispering-gallery-mode (WGM) disk resonators [32]. An emitter embedded in such structures shows enhanced emission brightness, by the Purcell effect [33], which is an important requirement for single photon sources useful for technologies [20, 21]. Now, the signature of single photon emission is the observation of antibunching in the second-order coherence ($g^{(2)}(\tau)$) function, which can be measured by performing the Hanbury Brown Twiss (HBT) experiment [34]. From the nature and quantitative properties of $g^{(2)}(\tau)$, vital information can be extracted such as the emitter's energy level structure [35]. Further, the radiative lifetime of these emitters provides a measure of the rate of photon generation from the single photon source.

The antibunching dip $g^{(2)}(0)$ is < 0.5 for single photon emitters (experimental bound) and > 0.5 for multiple emitters (general case) [36, 37]. Theoretically, for n non-interacting emitters with equal brightness $g^{(2)} = 1 - \frac{1}{n}$, thus for $n = 2$, $g^{(2)}(0) = 0.5$ [38]. However, for two interacting emitters, when the emitters are placed closer than the wavelength of light, the functional form of $g^{(2)}(\tau)$ can change due to the splitting of energy levels.

Here, we report the behaviour of the second-order correlation function for two solid-state emitters (namely, nitrogen-vacancy - NV centers in diamond) confined in a small volume (\ll wavelength of the optical excitation). We study the dissipative dynamics of the system to describe the reduction of lifetimes and discuss the possibility of superradiance (a collective phenomenon arising

from indistinguishable quantum emitters w.r.t to the optical field [39, 40]) from the system. We solve the Lindblad master equation for three cases: single NV center, two non-interacting NV centers and two interacting NV centers via dipole-dipole coupling. We experimentally verify the behaviour of the second-order correlation function for two NV center in an optical cavity, exhibiting cooperative effects (superradiance). Finally, we discuss the entropy of quantum random number generators using the coupled emitter system and compare it with single emitters.

II. THEORETICAL BACKGROUND

A. Nitrogen Vacancy (NV) centers

We consider the negatively charged nitrogen vacancy (NV⁻) centers in diamond (schematically shown in Fig. 1 (a)). In the tight-binding model, it consists of 6 valence electrons that can be described by 2-hole wavefunctions. First, we derive the one-hole wavefunctions for the system. The vacancy results in the appearance of four dangling orbitals - three from carbons and one from nitrogen, each being the lowest-energy solution of a single-electron Schrödinger equation with a potential from nuclei and bonded electrons - unknown but satisfying the C_3 symmetry of the defect. Let us denote these 3 carbon orbitals and one nitrogen orbital as $\sigma_1, \sigma_2, \sigma_3$ and σ_N , respectively.

In the tight-binding model, the electron system of the diamond crystal is described by the sum of covalent interactions between valence electrons of 2 nearest neighbour atoms. In the presence of defects with vacancies, the absence of a carbon ion will lead to the interaction between the electron from the substitutional atom and the ion via Coulomb interaction. The single-hole Hamiltonian takes in the $\{\sigma_1, \sigma_2, \sigma_3, \sigma_N\}$ basis a most general form allowed by the symmetry of the defect [41]:

$$V = V_N |\sigma_N\rangle\langle\sigma_N| + \sum_i \{V_C |\sigma_i\rangle\langle\sigma_i| + (h_N |\sigma_i\rangle\langle\sigma_N| + h.c.)\} + \sum_{i>j} h_C |\sigma_i\rangle\langle\sigma_j| + h.c. \quad (1)$$

$$= \begin{pmatrix} V_C & h_C & h_C & h_N \\ h_C & V_C & h_C & h_N \\ h_C & h_C & V_C & h_N \\ h_N^* & h_N^* & h_N^* & V_N \end{pmatrix} \quad (2)$$

where V_C is the Coulomb interaction of the carbon orbital at site i . h_C is the expectation value of the interaction between σ_i and σ_{i+1} . h_N is the interaction between σ_i and σ_N . h_N is the interaction between σ_N and σ_i .

Now considering the 3×3 upper block of the matrix in Eq. 2, we have:

$$V_{3 \times 3} = \begin{pmatrix} V_C & h_C & h_C \\ h_C & V_C & h_C \\ h_C & h_C & V_C \end{pmatrix} = (V_C - h_C)\mathbf{I} + 3h_C\mathbf{P} \quad (3)$$

where \mathbf{I}, \mathbf{P} are the 3×3 identity and projection matrices. $\mathbf{P} = 3(\frac{1}{3}\mathbf{1}^T\mathbf{1})$, where $\mathbf{1}$ are matrices of ones. The eigenvalues of $(V_C - h_C)\mathbf{I}$ and $3h_C\mathbf{P}$ are $\{V_C - h_C, V_C - h_C, V_C - h_C\}$ and $\{0, 0, 3h_C\}$, respectively. Thus, the eigenvalues and eigenvectors of $V_{3 \times 3}$ are $\{V_C - h_C, V_C - h_C, V_C + 2h_C\}$ and $\left\{ \frac{1}{\sqrt{3}} \begin{pmatrix} 1 \\ 1 \\ 1 \end{pmatrix}, \frac{1}{\sqrt{6}} \begin{pmatrix} 2 \\ -1 \\ -1 \end{pmatrix}, \frac{1}{\sqrt{2}} \begin{pmatrix} 0 \\ 1 \\ -1 \end{pmatrix} \right\}$, respectively. In this basis, we can rewrite the matrix in Eq. 2 as:

$$V = \begin{pmatrix} V_C + 2h_C & 0 & 0 & \sqrt{3}h_N \\ 0 & V_C - h_C & 0 & 0 \\ 0 & 0 & V_C - h_C & 0 \\ \sqrt{3}h_N^* & 0 & 0 & V_N \end{pmatrix} \quad (4)$$

which has a block-diagonal form. Thus, we have the doubly-degenerate eigenvalue $V_C - h_C$ corresponds to the eigensubspace $\text{span}\{\frac{1}{\sqrt{6}}(2\sigma_1 - \sigma_2 - \sigma_3), \frac{1}{\sqrt{2}}(\sigma_2 - \sigma_3)\}$. Now, we consider the reduced matrix:

$$V_{2 \times 2} = \begin{pmatrix} V_C + 2h_C & \sqrt{3}h_N \\ \sqrt{3}h_N^* & V_N \end{pmatrix} \quad (5)$$

in the subspace $\{\sigma_C (\equiv \frac{1}{3}(\sigma_1 + \sigma_2 + \sigma_3)), \sigma_N\}$. The characteristic polynomial of the matrix is:

$$\det(V_{2 \times 2} - \lambda\mathbf{I}_2) = \lambda^2 - (V_C + 2h_C + V_N)\lambda + V_N(V_C + 2h_C) - 3|h_N|^2 = 0 \quad (6)$$

(where \mathbf{I}_2 is the 2×2 identity matrix). On solving the characteristic polynomial given in Eq. 6, we obtain the eigenvalues (λ_{\pm}):

$$\lambda_{\pm} = \frac{1}{2} \left[(V_C + 2h_C + V_N) \pm \sqrt{(V_C + 2h_C - V_N)^2 + 12|h_N|^2} \right] = \frac{1}{2} [a + b \pm \Delta] \quad (7)$$

where, $a = V_C + 2h_C, b = V_N, \Delta = \sqrt{(a - b)^2 + 4|c|^2}, c = \sqrt{3}h_N$. The corresponding orthogonal eigenvectors are found to be:

$$v_- = \begin{pmatrix} \frac{-2c}{a-b+\Delta} \\ 1 \end{pmatrix} \quad (8)$$

$$v_+ = \begin{pmatrix} \frac{-2c}{a-b-\Delta} \\ 1 \end{pmatrix} \quad (9)$$

On normalizing the eigenvectors in Eqs. 8 and 9, we obtain the orthonormal eigenbasis of the matrix in Eq. 5:

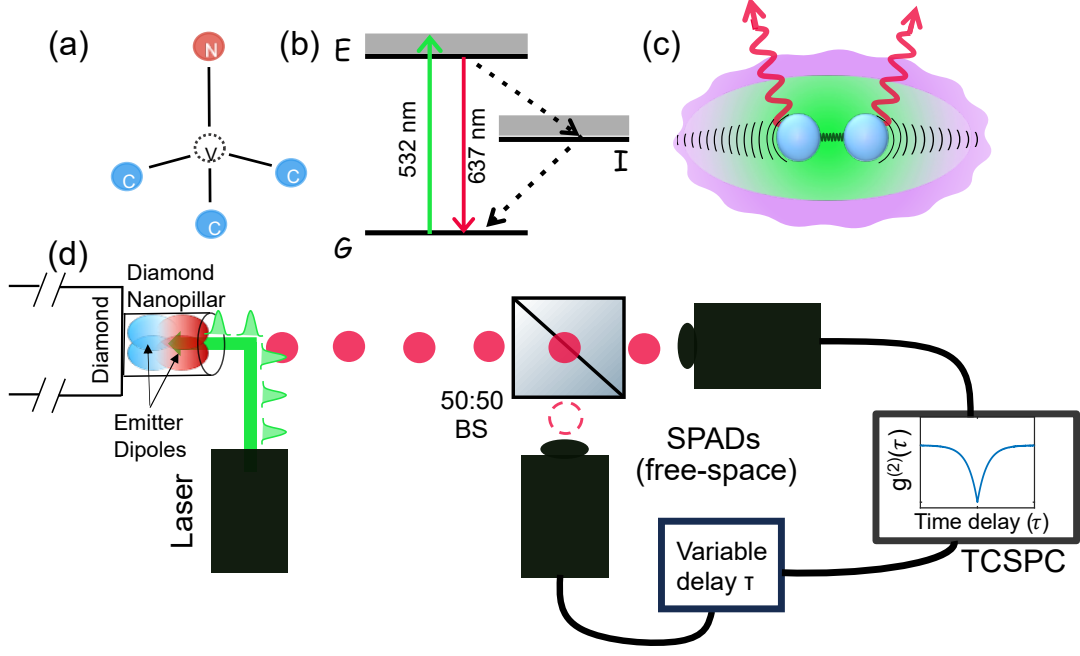


FIG. 1. (a) Schematic of the NV center defect in diamond. (b) Three-level energy structure of an NV center. G, I, E denote the ground, intermediate and excited states. The dashed lines indicate non-radiative transitions. The shaded regions indicate the vibronic levels of the excited and intermediate states. (c) Pictorial representation of two coupled NV centers (solid blue circles) in a common photonic bath (electric field in green) and phononic bath (purple). The red squiggly arrows represent the radiative emissions from the emitters. (d) The simplified experimental scheme depicts the Hanbury-Brown Twiss experiment performed for our system. The coupled emitters, embedded in a diamond nanopillar, are perturbed using a laser emitting at 532 nm wavelength and the emission is split using a 50:50 beam-splitter (BS) and sent to two detectors – single-photon avalanche diodes (SPADs). The coincidences (as a function of detection delay on one of the detectors) from the two detectors are measured using a time-correlated single photon counter (TCSPC). An exemplar plot for the normalized coincidences ($g^{(2)}(\tau)$) vs. time delay (τ) for a single emitter is shown as an inset figure on the TCSPC.

$$|v\rangle_- = \begin{pmatrix} \frac{-c}{\sqrt{\Delta(\frac{a-b+\Delta}{2})}} \\ \sqrt{\frac{a-b+\Delta}{2\Delta}} \end{pmatrix} = \begin{pmatrix} \frac{-\sqrt{3}h_N}{\sqrt{\Delta(\frac{V_C+2h_C-V_N+\Delta}{2})}} \\ \sqrt{\frac{V_C+2h_C-V_N+\Delta}{2\Delta}} \end{pmatrix} = \begin{pmatrix} \alpha_1 \\ \beta_1 \end{pmatrix} \quad (10)$$

$$|v\rangle_+ = \begin{pmatrix} \frac{c}{\sqrt{\Delta(\frac{\Delta-a+b}{2})}} \\ \sqrt{\frac{\Delta-a+b}{2\Delta}} \end{pmatrix} = \begin{pmatrix} \frac{\sqrt{3}h_N}{\sqrt{\Delta(\frac{\Delta-V_C-2h_C+V_N}{2})}} \\ \sqrt{\frac{\Delta-V_C-2h_C+V_N}{2\Delta}} \end{pmatrix} = \begin{pmatrix} \alpha_2 \\ \beta_2 \end{pmatrix} \quad (11)$$

where $\Delta = \sqrt{(V_C + 2h_C - V_N)^2 - 12|h_N|^2}$. Thus, we get a linearly independent set of 4 orthonormal vectors (single electron orbitals):

$$a_1 = \alpha_1 \frac{1}{3}(\sigma_1 + \sigma_2 + \sigma_3) + \beta_1 \sigma_N \quad (12)$$

$$a'_1 = \alpha_2 \frac{1}{3}(\sigma_1 + \sigma_2 + \sigma_3) + \beta_2 \sigma_N \quad (13)$$

$$e_x = \frac{1}{\sqrt{6}}(2\sigma_1 - \sigma_2 - \sigma_3) \quad (14)$$

$$e_y = \frac{1}{\sqrt{2}}(\sigma_2 - \sigma_3) \quad (15)$$

Now, from the single electron orbitals, we can estimate the energy levels of a 2-particle system. The 4 orbitals can be occupied by 8 electrons (from Hund's rule). Thus, the six-electron system of NV^- can be imagined as a 2-hole system. The spatial part of the two-hole orbitals can be calculated using:

$$\Psi_r = \frac{l_r}{h} \sum_e \chi_e^r(R_e \otimes R_e)(\phi_1 \otimes \phi_2) \quad (16)$$

where ϕ_1, ϕ_2 are single electron orbitals [see Eqs. 12 - 15]. R_e, h, l_r are the elements, order and the r th dimension of the irrep of C_{3v} group, respectively. The C_{3v} group consists of the identity element, rotations by $\pm \frac{2\pi}{3}$, and reflections in 3 vertical planes passing through each of the carbon atoms. We find that e_x, e_y transform as the non-trivial (E) representation whereas a_1, a_2 transform as the trivial (A_1) representation. We consider the spins of each hole as α (spin-up) and β (spin-down). Now using the spatial part of $\{a_1, a'_1, e_x, e_y\} \otimes \{a_1, a'_1, e_x, e_y\}$, obtained using Eq. 16, we add the spin parts after antisymmetrization of the spatial parts as required such that, the total wavefunction is antisymmetric. Through this procedure, we get 28 states in the $C_1^4 \otimes C_1^2 \otimes C_2^4 \otimes C_2^2$ space,

considering both spatial and spin components. Each of these states belongs to an irrep of the C_{3v} double group. Since transitions are allowed between states belonging to the same representation, we choose the three levels of ground ($|g\rangle$), intermediate ($|i\rangle$), and excited ($|e\rangle$) states [see Fig. 1 (b)] such that these levels belong to the unit irrep of the C_{3v} double group. The following are the three states:

$$\begin{aligned} |g\rangle &= \frac{1}{2}(e_x \otimes e_y - e_y \otimes e_x) \otimes (\uparrow \otimes \downarrow + \downarrow \otimes \uparrow) \\ |i\rangle &= \frac{1}{2}(e_x \otimes e_x + e_y \otimes e_y) \otimes (\uparrow \otimes \downarrow - \downarrow \otimes \uparrow) \\ |e\rangle &= |E_- \rangle \otimes |\uparrow\uparrow\rangle - |E_+ \rangle \otimes |\downarrow\downarrow\rangle \end{aligned} \quad (17)$$

where $|E_{\pm}\rangle = |a_1 e_{\pm} - e_{\pm} a_1\rangle$ and $e_{\pm} = \mp(e_x \pm i e_y)$ [41]. The transitions from $|g\rangle$ to $|e\rangle$ and vice versa are in the visible light range. Whereas, the transitions from $|e\rangle$ to $|i\rangle$ and $|i\rangle$ to $|g\rangle$ are non-radiative in nature. To obtain emission, the NV^- is first perturbed from the ground state using a light of wavelength 532 nm which is of higher energy than the energy gap between $|g\rangle$ and $|e\rangle$. At room temperature, the excited state possesses many vibronic levels. These energy levels have an energy separation which is much smaller than the energy of light. The higher energy excitation is provided to the system to ensure its transition to the excited state. Further, transitions in the vibrational levels to get to the excited ground vibronic state occur within ~ 100 ps \ll excited state lifetime. Thus, we can neglect the transitions occurring within the vibrational levels.

B. Dynamical Master Equation

To describe the dynamics of an emitter/ a system of emitters in an electric field, we define the master equation for the system. Then we find the behaviour of the second-order autocorrelation function in terms of the Lindblad operators.

The evolution of the density operator is given by the dynamical master equation [42]:

$$\begin{aligned} \frac{d\hat{\rho}}{dt} &= \frac{i}{\hbar}[\hat{\rho}, \hat{H}_0] - \sum_{i,j} \left[\gamma_{ij}(\omega_{eg})(\hat{\sigma}_j(\omega_{eg})\hat{\rho}\hat{\sigma}_i^\dagger(\omega_{eg}) \right. \\ &\quad - \{\hat{\sigma}_i^\dagger(\omega_{eg})\hat{\sigma}_j(\omega_{eg}), \hat{\rho}\}) + \sum_{\omega} \Gamma_{ij}(\omega)(\hat{\sigma}_j(\omega)\hat{\rho}\hat{\sigma}_i^\dagger(\omega) \\ &\quad \left. - \{\hat{\sigma}_i^\dagger(\omega)\hat{\sigma}_j(\omega), \hat{\rho}\}) \right] \equiv \hat{\mathcal{L}}\hat{\rho} \end{aligned} \quad (18)$$

where \hat{H}_0 denotes the Hamiltonian of the reversible part of the dynamics and $\gamma_{ij}(\omega_{eg})$ and $\Gamma_{ij}(\omega)$ denote the rates of irreversible processes for photonic and phononic transitions, respectively. The jump operators and rates are described for particular transition frequencies ω_{eg} (photonic) and $\omega \in \{\omega_{ig}, \omega_{ei}\}$ (phononic). Finally, i and j denote the number of emitters in the system, i.e., $i, j \in \{1, 2\}$.

To derive the rates of thermalization ($\gamma(\omega_{eg})$) for our experimental setup, we consider the radiation field as the bath and a system of single or two emitters [see Figs. 1 (c) and (d)]. The interaction Hamiltonian is given as:

$$H_I = \sum_{j=1}^2 (\hat{\sigma}_j \vec{d} \cdot \vec{E}(\vec{r}_j) + \hat{\sigma}_j^\dagger \vec{d}^* \cdot \vec{E}(\vec{r}_j)) \quad (19)$$

where the dipole operator is $\vec{D}_j = \vec{d}(\hat{\sigma}_j^\dagger + \hat{\sigma}_j)$ represents the dipole operator of the j -th atom, and \vec{d} is the dipole matrix element of the transition.

Consider the reservoir electric field at position \vec{r}_i as:

$$\vec{E}(\vec{r}_i) = \sum_{k,\lambda} \sqrt{\frac{2\pi\omega_k}{V}} \vec{e}_\lambda(\vec{k}) (b_\lambda(\vec{k}) e^{i\vec{k}\cdot\vec{r}_i} - b_\lambda^\dagger(\vec{k}) e^{-i\vec{k}\cdot\vec{r}_i}) \quad (20)$$

The thermalization rates can be calculated using the bath correlation function:

$$\gamma_{ij}(\omega) = \int_{-\infty}^{\infty} dt \exp\{i\omega t\} \langle \vec{d}^* \cdot \vec{E}(\vec{r}_i, t) \vec{d} \cdot \vec{E}(\vec{r}_j, 0) \rangle \quad (21)$$

The inner products of the electric field operators depend on the bath state (ρ_B). Let $\rho_B = \prod_{k,\lambda} (1 - e^{-\beta\hbar\omega_k}) e^{-\beta\hbar\omega_k b_\lambda^\dagger b_\lambda} + |\alpha\rangle\langle\alpha|_{k_\alpha, \lambda_\alpha}$ and $N(\omega_k) = \frac{1}{e^{\beta\hbar\omega_k} - 1}$. As the experiment is conducted at room temperature and a coherent laser field is applied to perturb the system, the bath combines thermal and coherent states. The coherent state signifies the pump field whereas the thermal state signifies all other radiation due to emission and non-zero temperature.

Since the system is perturbed using laser light of a particular mode and polarisation, we represent it using the coherent state $|\alpha\rangle\langle\alpha|_{k_\alpha, \lambda_\alpha}$ with $\lambda_\alpha = 532$ nm (excitation wavelength). All other radiation representing the finite temperature at which the experiment is conducted and the emission from the system is contained in the first term of ρ_B .

In general:

$$\langle b_\lambda(\vec{k}) b_{\lambda'}(\vec{k}') \rangle = \langle b_\lambda^\dagger(\vec{k}) b_{\lambda'}^\dagger(\vec{k}') \rangle = 0 \quad (22)$$

$$\langle b_\lambda^\dagger(\vec{k}) b_{\lambda'}(\vec{k}') \rangle = \delta_{kk'} \delta_{\lambda\lambda'} \bar{n} \quad (23)$$

$$\langle b_\lambda(\vec{k}) b_{\lambda'}^\dagger(\vec{k}') \rangle = \delta_{kk'} \delta_{\lambda\lambda'} (1 + \bar{n}) \quad (24)$$

For the thermal and coherent state $\bar{n} = N(\omega)$ and $\bar{n} = |\alpha|^2$, respectively. Using the expressions for \vec{E} in Eq. 21, we obtain the rates of thermalization for a given ω as [for derivation refer to Appendices A and B]:

$$\begin{aligned}
\gamma_{ij}(\omega) &= \frac{4\omega^3 d^2}{3c^3} f\left(\frac{\omega}{c}|r_i - r_j|, \theta_{ij}\right)(1 + N(\omega)) \\
&+ \frac{2\pi^2 \omega |d_\alpha|^2}{L^3} (1 - 2|\alpha|^2) \\
&+ id^2 P \int_0^\infty d\omega_k \omega_k^3 f(x_{ij}, \theta_{ij}) \left(\frac{1 + N(\omega_k)}{\omega - \omega_k} + \frac{N(\omega_k)}{\omega + \omega_k} \right) \\
&- i \frac{2\pi \omega_\alpha}{L^3} |d_\alpha|^2 \left(|\alpha|^2 P \frac{1}{\omega_\alpha + \omega} + (1 + |\alpha|^2) P \frac{1}{\omega_\alpha - \omega} \right)
\end{aligned} \tag{25}$$

where ω_α, d_α correspond to the frequency and dipole moment along the polarisation of the pump field, respectively. Also, $f(x_{ij}, \theta_{ij}) = j_0(x_{ij}) + P_2(\cos \theta_{ij})j_2(x_{ij})$, $x_{ij} = \frac{\omega_k}{c}|r_i - r_j|$ and $\cos \theta_{ij} = \frac{|\vec{d}_i(\vec{r}_i - \vec{r}_j)|^2}{d^2|\vec{r}_i - \vec{r}_j|^2}$. j_0 and P_2 are the Bessel function of 0-th order and Legendre polynomial of 2nd order, respectively [details in Appendix A].

C. Second-order autocorrelation function

In terms of the jump operators $\{\hat{\sigma}, \hat{\sigma}^\dagger\}$, the second-order autocorrelation function is given by [40, 43]:

$$g^{(2)}(\tau) = \sum_{i,j=1}^2 \frac{\langle \hat{\sigma}_i^\dagger(0) \hat{\sigma}_i^\dagger(\tau) \hat{\sigma}_j(\tau) \hat{\sigma}_j(0) \rangle}{\langle \hat{\sigma}_i^\dagger(0) \hat{\sigma}_j(0) \rangle \langle \hat{\sigma}_i^\dagger(\tau) \hat{\sigma}_j(\tau) \rangle} \tag{26}$$

where τ is given as the time delay in detection between two detections after the beam-splitter in the experimental setup. The solution to Eq. 18 can be given as:

$$\hat{\rho}(t) = \exp(\hat{\mathcal{L}}t) \hat{\rho}(0) \tag{27}$$

where $\hat{\mathcal{L}}$ is the Lindbladian of Eq. 18. Now, we consider the following three cases:

1. One NV center

Here we consider the free Hamiltonian as $\hat{H}_0 = \sum_r E_r |r\rangle\langle r|$ and the jump operators for a transition frequency ω_{lm} as $\hat{\sigma}(\omega_{lm}) = |l\rangle\langle m|$. E_r s represent the eigenenergies of the system. In the $\{|g\rangle, |i\rangle, |e\rangle\}$, i.e., the eigenbasis of NV centers we evaluate the evolution of the diagonal and off-diagonal elements of $\hat{\rho}$.

Let elements of $\frac{d\hat{\rho}}{dt}$ be $\sum_{p,q} \dot{\rho}_{pq} |p\rangle\langle q|$. Then using the forms for \hat{H}_0 and $\hat{\sigma}(\omega_{lm})$ in Eq. 18 we can write:

$$\begin{aligned}
\sum_{p \neq q} \dot{\rho}_{pq} |p\rangle\langle q| &= \frac{1}{i\hbar} \sum_r \sum_{p,q} E_r \rho_{pq} [|r\rangle\langle r|, |p\rangle\langle q|] + \left(\sum_{l \neq m = \{e,g\}} |\langle l|z|m\rangle|^2 \gamma(\omega_{lm}) + \sum_{l \neq m = \{g,i,e\}} h_{lm} \Gamma(\omega_{lm}) \right) \sum_{p,q} \rho_{pq} (|l\rangle\langle m| |p\rangle\langle q| |m\rangle\langle l| \\
&- \frac{1}{2} \{ |m\rangle\langle m|, |p\rangle\langle q| \}) \\
&= \frac{1}{i\hbar} \sum_r \sum_{p,q} E_r \rho_{pq} (\delta_{rp} |r\rangle\langle q| + \delta_{rq} |p\rangle\langle r|) + \left(\sum_{l \neq m = \{e,g\}} |\langle l|z|m\rangle|^2 \gamma(\omega_{lm}) + \sum_{l \neq m = \{g,i,e\}} h_{lm} \Gamma(\omega_{lm}) \right) \times \\
&\sum_{p,q} \rho_{pq} \left(\delta_{mp} \delta_{qm} |l\rangle\langle l| - \frac{1}{2} (\delta_{mp} |m\rangle\langle q| + \delta_{mq} |p\rangle\langle m|) \right) \\
&= \frac{1}{i\hbar} \sum_{p,q} (E_p - E_q) \rho_{pq} |p\rangle\langle q| + \left(\sum_{l \neq m = \{e,g\}} |\langle l|z|m\rangle|^2 \gamma(\omega_{lm}) + \sum_{l \neq m = \{g,i,e\}} h_{lm} \Gamma(\omega_{lm}) \right) \rho_{mm} |l\rangle\langle l| \\
&- \frac{1}{2} \left(\sum_{m \neq q = \{e,g\}} |\langle q|z|m\rangle|^2 \gamma(\omega_{mq}) + \sum_{m \neq q = \{g,i,e\}} h_{mq} \Gamma(\omega_{mq}) \right) \rho_{mq} |m\rangle\langle q| \\
&- \frac{1}{2} \left(\sum_{m \neq p = \{e,g\}} |\langle p|z|m\rangle|^2 \gamma(\omega_{pm}) + \sum_{m \neq p = \{g,i,e\}} h_{pm} \Gamma(\omega_{pm}) \right) \rho_{pm} |p\rangle\langle m|
\end{aligned} \tag{28}$$

In the case of the diagonal elements, i.e., $\sum_{p=q} \dot{\rho}_{pq} |p\rangle\langle q| \equiv \sum_p \dot{\rho}_{pp} |p\rangle\langle p|$, we compare the coefficients of $|p\rangle\langle p|$ on both sides of Eq. 28 and get:

$$\begin{aligned}
\dot{\rho}_{pp} &= - \left(\sum_{l \neq p = \{e,g\}} |\langle l|z|p\rangle|^2 \gamma(\omega_{lp}) + \sum_{l \neq p = \{g,i,e\}} h_{lp} \Gamma(\omega_{lp}) \right) \rho_{pp} \\
&+ \left(\sum_{m \neq p = \{e,g\}} |\langle p|z|m\rangle|^2 \gamma(\omega_{pm}) + \sum_{m \neq p = \{g,i,e\}} h_{pm} \Gamma(\omega_{pm}) \right) \rho_{mm}
\end{aligned} \tag{29}$$

From the properties of Davies operators [42], we know that the diagonal and off-diagonal elements of the density matrix $\hat{\rho}$ evolve independently. To understand the dynamics of the emitters we need the rate equations concerning only the diagonal elements of $\hat{\rho}$. Thus, the rate equations are given by:

$$\begin{pmatrix} \dot{\rho}_g \\ \dot{\rho}_i \\ \dot{\rho}_e \end{pmatrix} = R \begin{pmatrix} \rho_g \\ \rho_i \\ \rho_e \end{pmatrix} \quad (30)$$

where,

$$R = \begin{pmatrix} -h_{gi}\Gamma(\omega_{ig}) - |\langle g|z|e\rangle|^2\gamma(\omega_{eg}) & h_{gi}\Gamma(-\omega_{ig}) & |\langle g|z|e\rangle|^2\gamma(-\omega_{eg}) \\ h_{gi}\Gamma(\omega_{ig}) & -h_{gi}\Gamma(-\omega_{ig}) - h_{ie}\Gamma(\omega_{ei}) & h_{ie}\Gamma(-\omega_{ei}) \\ |\langle g|z|e\rangle|^2\gamma(\omega_{eg}) & h_{ie}\Gamma(\omega_{ei}) & -h_{ie}\Gamma(-\omega_{ei}) - |\langle g|z|e\rangle|^2\gamma(\omega_{-eg}) \end{pmatrix} \quad (31)$$

Denoting the $|\langle l|z|m\rangle|^2\gamma(\omega_{lm}), h_{lm}\Gamma(\omega_{lm})$ as r_{lm} , and using $\gamma(-\omega_{lm}) = \gamma(\omega_{ml})$ and $\Gamma(-\omega_{lm}) = \Gamma(\omega_{ml})$, we can write the following system of linear equations for $\{\dot{\rho}_g, \dot{\rho}_i, \dot{\rho}_e\}$:

$$\begin{pmatrix} \dot{\rho}_g \\ \dot{\rho}_i \\ \dot{\rho}_e \end{pmatrix} = \begin{pmatrix} -(r_{ig} + r_{eg}) & r_{gi} & r_{ge} \\ r_{ig} & -(r_{gi} + r_{ei}) & r_{ie} \\ r_{eg} & r_{ei} & -(r_{ie} + r_{ge}) \end{pmatrix} \begin{pmatrix} \rho_g \\ \rho_i \\ \rho_e \end{pmatrix} \quad (32)$$

For finite temperatures such as 300 K, $r_{ie} = 0 = r_{gi}$, thus we get:

$$\begin{pmatrix} \dot{\rho}_g \\ \dot{\rho}_i \\ \dot{\rho}_e \end{pmatrix} = \begin{pmatrix} -(r_{ig} + r_{eg}) & 0 & r_{ge} \\ r_{ig} & -r_{ei} & 0 \\ r_{eg} & r_{ei} & -r_{ge} \end{pmatrix} \begin{pmatrix} \rho_g \\ \rho_i \\ \rho_e \end{pmatrix} \quad (33)$$

By evaluating the nullspace and eigen-decomposition of the 3×3 matrix in Eq. 33, one can obtain the second-order autocorrelation function. Following the procedure highlighted in [35], under the condition $r_{ig} + r_{ei} \ll r_{eg}$, the eigenvalues of the 3×3 matrix are:

$$\lambda_1 = r_{eg} + r_{ge} \quad (34)$$

$$\lambda_2 = r_{ei} + \frac{r_{ig}r_{ge}}{r_{eg} + r_{ge}} \quad (35)$$

$$\lambda_3 = 0 \quad (36)$$

Let us denote the matrix of eigenvectors of R as R_{evec} . Then one can write:

$$\begin{pmatrix} \rho_g \\ \rho_i \\ \rho_e \end{pmatrix} = R_{\text{evec}} \begin{pmatrix} \exp(-\lambda_1 t) \\ 1 \\ \exp(-\lambda_2 t) \end{pmatrix} \quad (37)$$

We have (from Eq. 26):

$$g^{(2)}(\tau) = \frac{p_e(t, g; \tau)}{p_e(\infty)} = \frac{(0 \ 0 \ 1) \begin{pmatrix} \rho_g \\ \rho_i \\ \rho_e \end{pmatrix}}{(0 \ 0 \ 1) \text{Nullspace}[R_{\text{evec}}]} \quad (38)$$

Using the initial condition $\rho_g = 1; \rho_e = 0 = \rho_i$ for evaluating $p_e(t, g; \tau)$, we get:

$$g^{(2)}(\tau) = 1 - (1 + a) \exp(-\lambda_1 \tau) + a \exp(-\lambda_2 \tau) \quad (39)$$

where $a = \frac{r_{ge}r_{ig}}{r_{ei}(r_{eg} + r_{ge})}$. From Eq. 39, we find that $g^{(2)}(\tau) = 0$ for $\tau = 0$ and $g^{(2)}(\tau) \rightarrow 1$ asymptotically (as expected for a single emitter).

2. Two NV centers without interaction

Next, we consider a system of two NV centers such that there is no interaction between these two emitters. Then, the free Hamiltonian becomes $\hat{H}_0 = \sum_r E_r (|r\rangle\langle r| \otimes I + I \otimes |r\rangle\langle r|)$. The jump operators for the first and second NV center at transition frequency ω_{lm} are $\hat{\sigma}_1(\omega_{lm}) = |l\rangle\langle m| \otimes I$ and $\hat{\sigma}_2(\omega_{lm}) = I \otimes |l\rangle\langle m|$.

In this case, to evaluate the dynamics of the state of the system in the eigenbasis of \hat{H}_0 , we act with $\hat{\mathcal{L}}$ on the vectorized $\hat{\rho} = \sum_{p_1, q_1, p_2, q_2} \rho_{p_1 q_1 p_2 q_2} |p_1 q_1\rangle\langle p_2 q_2|$, where $p_1, q_1, p_2, q_2 \in \{1, 2, 3\}$. This yields an 81×81 block diagonal matrix $\hat{\mathcal{L}}$. The block structure of this matrix is of the form (dimension: no. of blocks):

$$1 \times 1 : 6, 2 \times 2 : 6, 8 \times 8 : 6, 15 \times 15 : 1$$

. Interestingly, we observed that the populations and coherence of the system mix. Thus, one cannot describe the evolution of the diagonal (populations) terms of $\hat{\rho}$ as separate from the off-diagonal (coherences) terms and write the rate equations for the populations of various energy levels. Interestingly, we observed that the populations

and coherence of the system mix. Thus, one cannot describe the evolution of the diagonal (populations) terms of $\hat{\rho}$ as separate from the off-diagonal (coherences) terms and write the rate equations for the populations of various energy levels.

The matrix of 9×9 of $\hat{\rho}$ is given by:

$$\hat{\rho} = \begin{matrix} & \begin{matrix} gg & gi & ge & ig & ii & ie & eg & ei & ee \end{matrix} \\ \begin{matrix} gg \\ gi \\ ge \\ ig \\ ii \\ ie \\ eg \\ ei \\ ee \end{matrix} & \begin{matrix} \bullet & \blacksquare & \star & \blacksquare & \bullet & \blacklozenge & \star & \blacklozenge & \bullet \\ \times & \bullet & \bullet & \bullet & \blacksquare & \star & \bullet & \star & \bullet \\ \blacklozenge & + & \bullet & + & \star & \blacksquare & \bullet & \blacksquare & \star \\ \times & \bullet & \bullet & \bullet & \blacksquare & \star & \bullet & \star & \bullet \\ \bullet & \times & \times & \times & \bullet & \bullet & \times & \bullet & \bullet \\ \blacklozenge & + & \times & + & \star & \blacksquare & \bullet & \bullet & \bullet \\ \blacklozenge & + & \bullet & + & \star & \blacksquare & \bullet & \bullet & \star \\ \blacklozenge & + & \times & \times & \bullet & \bullet & \times & \bullet & \bullet \\ \bullet & \times & \blacklozenge & \blacklozenge & \bullet & \bullet & \times & \bullet & \bullet \\ \bullet & \times & \blacklozenge & \blacklozenge & \bullet & \bullet & \times & \bullet & \bullet \\ \bullet & \times & \blacklozenge & \blacklozenge & \bullet & \bullet & \times & \bullet & \bullet \\ \bullet & \times & \blacklozenge & \blacklozenge & \bullet & \bullet & \times & \bullet & \bullet \\ \bullet & \times & \blacklozenge & \blacklozenge & \bullet & \bullet & \times & \bullet & \bullet \\ \bullet & \times & \blacklozenge & \blacklozenge & \bullet & \bullet & \times & \bullet & \bullet \\ \bullet & \times & \blacklozenge & \blacklozenge & \bullet & \bullet & \times & \bullet & \bullet \end{matrix} \end{matrix}$$

For superradiance, the thermalization rates are equal for both the emitters ($\gamma_{ij} = \gamma, \Gamma_{ij}(\omega) = \Gamma(\omega), \omega \in \{\omega_{ig}, \omega_{ei}\} \forall i, j \in \{1, 2\}$) at each transition frequency ($\omega_{eg}, \omega_{ig}, \omega_{ei}$) [42], corresponding to radiative and non-radiative transitions. Due to the indistinguishability of emitters, the excited ($|e\rangle$) and ground ($|g\rangle$) states of the two emitters form antisymmetric: $\frac{1}{\sqrt{2}}(|eg - ge\rangle)$ and symmetric: $\frac{1}{\sqrt{2}}(|eg + ge\rangle)$ Dicke states. These states have energies between $|ee\rangle$ and $|gg\rangle$. As bright transitions occur from the symmetric Dicke state only [43], the following ladder operators can be defined: $\hat{\sigma}_1 = |eg + ge\rangle\langle gg|, \hat{\sigma}_2 = |ee\rangle\langle eg + ge|$.

First, we evaluate the numerator of Eq. 26. In the Heisenberg picture, the operator ($\hat{\sigma}(0)$) evolution in time is given by $\exp(\hat{\mathcal{L}}\tau)\hat{\sigma}(0)$. Using this we write:

$$g^{(2)}(\tau) = \sum_{i,j=1}^2 \frac{\langle \hat{\sigma}_i^\dagger(0)\hat{\sigma}_j^\dagger(\tau) \exp(\hat{\mathcal{L}}\tau)\hat{\sigma}_j(0)\hat{\sigma}_i(0) \rangle}{\langle \hat{\sigma}_i^\dagger(0)\hat{\sigma}_j(0) \rangle \langle \hat{\sigma}_i^\dagger(\tau)\hat{\sigma}_j(\tau) \rangle} \quad (40)$$

Thus, we evaluate $\sum_{i,j} \hat{\sigma}(0)\hat{\sigma}(0)$. We use definitions of $\hat{\sigma}_1$ and $\hat{\sigma}_2$ and find:

$$\begin{aligned} \sum_{i,j} \hat{\sigma}_i(0)\hat{\sigma}_j(0) &= \left(|eg + ge\rangle\langle gg| + |ee\rangle\langle eg + ge| \right)^2 \\ &= |ee\rangle\langle gg| \end{aligned} \quad (41)$$

Thus, we get $\sum_{i,j} \exp(\hat{\mathcal{L}}\tau)\hat{\sigma}_i(0)\hat{\sigma}_j(0) = \exp(\hat{\mathcal{L}}\tau)|ee\rangle\langle gg|$. Therefore, one must observe the dynamics of the operator $|ee\rangle\langle gg|$. Further, we can decompose $\hat{\sigma}_1$ and $\hat{\sigma}_2$ as sums of $|eg\rangle\langle gg|, |ge\rangle\langle gg|$ and $|ee\rangle\langle eg|, |ee\rangle\langle ge|$, respectively. Hence, in the block-diagonal matrix $\hat{\mathcal{L}}$, we restrict to evaluating $\exp(\hat{\mathcal{L}}\tau)$

of the block describing the evolution of the elements $|eg\rangle\langle gg|, |ge\rangle\langle gg|$ and $|ee\rangle\langle eg|, |ee\rangle\langle ge|$ of $\hat{\rho}$.

Interestingly, we find that the evolution of $|ee\rangle\langle gg|$ does not depend on the block of $\hat{\mathcal{L}}$ describing the diagonal entries of $\hat{\rho}$ (15×15). Instead, the operator dynamics is described by an 8×8 block. Since, the evolution of the operators $\hat{\sigma}_i \forall i \in \{1, 2\}$ does not depend on the block describing diagonal entries of $\hat{\rho}$, this must be a description of a non-classical behaviour, namely, superradiance. We identify that the blue diamonds in the matrix of $\hat{\rho}$ shown in Fig. II C 2 represent the dynamics in the operator subspace $\text{span}\{|ge\rangle\langle gg|, |ie\rangle\langle gi|, |ie\rangle\langle ig|, |eg\rangle\langle gg|, |ei\rangle\langle gi|,$

$|ei\rangle\langle ig|, |ee\rangle\langle ge|, |ee\rangle\langle eg|\}$. The block of Lindblad operator $\hat{\mathcal{L}}$ containing these elements is denoted by \hat{J} . The exponent of this matrix can be evaluated by finding the eigenvalues of this matrix and exponentiation them. Now to obtain the denominator of the Eq. 26, we first find the evolution of the operators in terms of the Lindbladian $\hat{\mathcal{L}}$.

$(\hat{\sigma}(\tau))^\dagger = \left(\exp(\hat{\mathcal{L}}\tau)\hat{\sigma}(0) \right)^\dagger = \hat{\sigma}^\dagger(0) \exp(\hat{\mathcal{L}}^\dagger\tau)$. Thus we get, $\langle \hat{\sigma}^\dagger(\tau)\hat{\sigma}(\tau) \rangle = \langle \hat{\sigma}^\dagger(0)\hat{\sigma}(0) \rangle$. Similar to the evaluation of the numerator, here we calculate $\hat{\sigma}^\dagger(0)\hat{\sigma}(0)$. This operator yields $|ee\rangle\langle ee|$. Thus, the evolution of the denominator of Eq. 26 is governed by the 11×11 block of the $\hat{\mathcal{L}}$ operator. Since there is no explicit time dependence in the denominator, the steady state probability of $\rho(\infty)_{ee,ee}$ gives the explicit form of $\hat{\sigma}^\dagger(0)\hat{\sigma}(0)$ for this system.

Thus we get:

$$g^{(2)}(\tau) = \frac{\sum_{i,j=1,4} \left([e^{\hat{J}\tau}]_{ii} [e^{\hat{J}\tau}]_{jj} + \sum_{i,j=7,8} [e^{\hat{J}\tau}]_{ii} [e^{\hat{J}\tau}]_{jj} \right)}{[\rho(\infty)]_{ee,ee}^2} \quad (42)$$

Thus, on diagonalizing \hat{J} , which is an 8×8 , one can extract its eigenvalues $\lambda_1, \dots, \lambda_6$. Further, using these λ s we can obtain the exponentiation of \hat{J} . Further, the nullspace of 11×11 block $\hat{\mathcal{L}}$ gives us $[\rho(\infty)]_{ee,ee}$.

From the structure of Eq. 42, we estimate the contribution of 6 exponentials to the $g^{(2)}(\tau)$ function (as opposed to 2 exponents for a single, three-level emitter). However, diagonalization of a symbolic 8×8 matrix is very difficult. While we were working on this article, a recent study was reported by Qu et al. [44], where the numerics depicting the $g^{(2)}(\tau)$ function have been performed for superradiance in 2 NV centers. In our later sections, we discuss our experimental results which also match with the expected behaviour of the $g^{(2)}(\tau)$ function from the study by Qu et al.

3. Two NV centers with dipole-dipole interaction

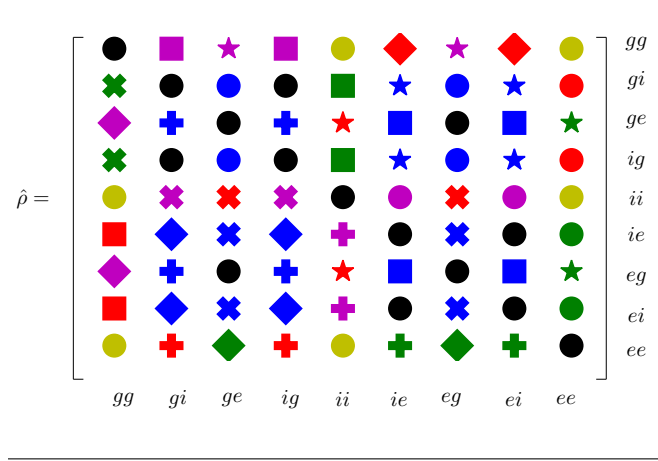
Next, we consider two NV centers interacting via dipole-dipole interactions. We consider the following dipole-dipole interaction [40]:

$$V = V_{eg}(|eg\rangle\langle ge| + |ge\rangle\langle eg|) + V_{ig}(|ig\rangle\langle gi| + |gi\rangle\langle ig|) + V_{ei}(|ei\rangle\langle ie| + |ie\rangle\langle ei|) \quad (43)$$

where $V_{ij}, i, j = \{g, i, e\}$ and $i \neq j$ signify the strength of dipolar transition from i th level to j th level. We add this interaction, thus, $H_0 \rightarrow H_0 + V$ (where H_0 is the same free Hamiltonian for 2 non-interacting NVs). We calculate the spectral decomposition for such a system and find that the number of distinct transition frequencies (ω s) are 9. Corresponding to this, we again act with $\hat{\mathcal{L}}$ on $\hat{\rho}$ as in Sec. II C 2, and find the block structure of the form (dimension: no. of blocks):

$$1 \times 1 : 6, 2 \times 2 : 18, 4 \times 4 : 6, 15 \times 15 : 1$$

. Following is the structure of $\hat{\rho}$:



$$\hat{J}_1 = \begin{pmatrix} a_1 & b_1 \\ b_1 & a_1 \end{pmatrix}; \hat{J}_2 = \begin{pmatrix} a_2 & b_2 \\ b_2 & a_2 \end{pmatrix} \quad (45)$$

where $a_i, b_i, i \in \{1, 2\}$ depend on the transition strengths d, h_{ig}, h_{ei} and thermalization rates $\gamma(\omega)$ and $\Gamma(\omega')$ (since for superradiance γ and Γ do not depend on i, j). Here, ω and ω' denote the sets of radiative and non-radiative transition frequencies, respectively. The eigenvalues of \hat{J}_1 and \hat{J}_2 are $a_1 \pm b_1$ and $a_2 \pm b_2$, respectively. Thus, the diagonals of $e^{\hat{J}_1 \tau}$ and $e^{\hat{J}_2 \tau}$ are given as $e^{(a_1 \pm b_1) \tau}$ and $e^{(a_2 \pm b_2) \tau}$, respectively. Therefore, from Eq. 44, we have:

$$g^{(2)}(\tau) = \frac{e^{a_1 \tau} (e^{b_1 \tau} e^{(a_2 + b_2) \tau} + e^{b_1 \tau} e^{(a_2 - b_2) \tau} + e^{-b_1 \tau} e^{(a_2 + b_2) \tau} + e^{-b_1 \tau} e^{(a_2 - b_2) \tau})}{[\rho(\infty)]_{ee, ee}^2} \quad (46)$$

This is a combination of 4 exponents instead of 6 (as for 2 NVs without interaction).

III. EXPERIMENTAL RESULTS & DISCUSSION

The sample (7 keV irradiated, single NV arrays from QZabre Ltd.) consists of a diamond membrane with nanopillar arrays, some containing single NVs, such that the collection efficiency is $10\times$ compared to bulk diamond.

A. Measurements of Various Emitter Properties

1. Time-Resolved Intensity

We perform a direct measurement of the fluorescence lifetime from the pillars containing single NV centers using pulsed excitation at a 20 MHz repetition rate with a pulse width of ≈ 200 ps. Note that the direct lifetime measurement corresponds to the total decay rate from the excited state including all possible decay paths (radiative and non-radiative). We show the time-resolved intensity decay measured for four pillars containing emitters in Fig. 2 (a) [dots]. These intensity decays are fitted using the following function:

$$I(t) = y_0 + a_1 e^{-t/t_1} + a_2 e^{-t/t_2} \quad (47)$$

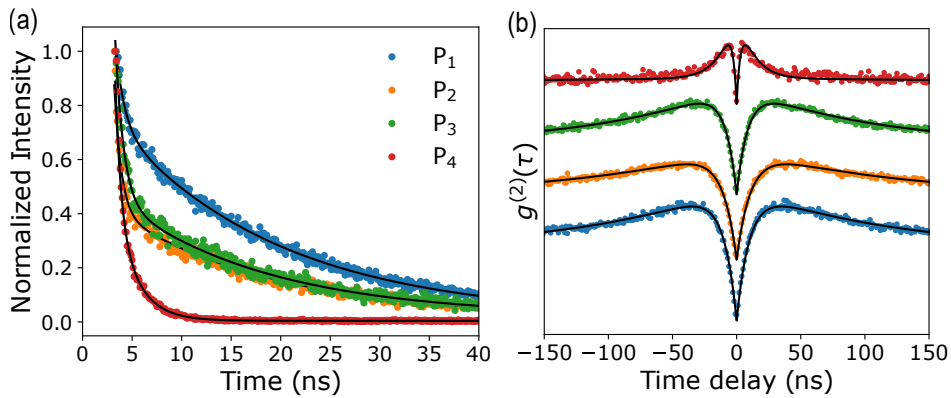


FIG. 2. **Comparison of fluorescence lifetimes and antibunching from various pillars:** (a) Time-resolved PL decay for four pillars containing NV centers (labelled as P_1, P_2, P_3 and P_4) (measured: dots; fitting with Eq. 47: solid line). P_4 shows a sharp decay with a time constant much smaller than the other emitters, indicating emission from two or more coupled emitters. (b) $g^{(2)}(\tau)$ (measured: dots; solid line for fitting with Eqs. 48 (for P_1, \dots, P_3) and 49 for P_4) as a function of time delay τ in detection of coincidences. For P_4 , the antibunching dip has a lower amplitude $g^{(2)}(0) > 0.5$, which can imply the presence of more than two emitters in P_4 .

where y_0 is the offset, a_1, a_2 are the amplitudes of the exponents with time constants t_1, t_2 , respectively. The decay occurring on timescales < 1 ns can be attributed to the background within the emitting crystal [45]. Thus, the principle time constant arising due to fluorescence decay from the emitters P_i , ($i \in \{1, 2, 3, 4\}$) are 16.6 ± 0.24 ns, 15.7 ± 0.36 ns, 14.7 ± 0.38 ns and 2.05 ± 0.03 ns, respectively. Note that the longer lifetime can be extracted by fitting a single exponential to the measured data for times greater than 1 ns. For the pillars P_1, \dots, P_3 , the fluorescence lifetime is close to the reported value for a single NV center, i.e., ≈ 12 ns. However, for P_4 , we observe a drastic reduction by 6 times, indicating some perturbative potential within which the emitter exists.

2. Hanbury-Brown Twiss Experiment

Next, to comment on the intensity correlations in the emitted light, we perform the Hanbury-Brown Twiss (HBT) experiment. From this experiment, we extract the second-order correlation function $g^{(2)}(\tau)$ w.r.t the delay in detection of coincidences (τ) between two SPADs [see Supplementary Information]. All the measurements described were conducted multiple times over various days to ensure repeatability. In Fig. 2 (b), we show the $g^{(2)}(\tau)$ vs. time delay τ for various pillars P_i stacked vertically with an offset. Single NV centers exhibit the three-level model owing to the intermediate metastable (singlet) state, we thereby use the following fitting function [see Sec. II C 1]:

$$g_{3-level}^{(2)}(\tau) = 1 - (1 + a)e^{-\tau/\tau_1} + ae^{-\tau/\tau_2} \quad (48)$$

where we use the modified version of Eq. 39, i.e., $1/\lambda_i = \tau_i$, $i \in \{1, 2\}$. We can see two characteristic time

constants in the $g^{(2)}(\tau)$, i.e., two exponential components. Depending on the transition rates from excited to intermediate to ground state, $g^{(2)}(\tau) > 1$ for $\tau > \tau_1$ then tending to the asymptote of 1 at $\tau \gg \tau_1$. We observe that for 3 pillars P_i , $i \in \{1, 2, 3\}$, the three-level equation for $g^{(2)}(\tau)$ fits well to the measured data. Further, the observed antibunching dips are below the experimental bound, i.e., $g^{(2)}(0) < 0.5$ for P_1, P_2, P_3 , indicating the emitted light is from a single emitter.

Interestingly, for pillar P_4 , we observe the certain unique properties of the $g^{(2)}(\tau)$ function. First, the amplitude of the antibunching dip is close to 0.8, i.e., $g^{(2)}(0) \rightarrow 0.8$. Since $g^{(2)}(0) > 0.5$, we consider the dynamics of this system to be similar to that of 2 NV centers. While fitting the behaviour of $g^{(2)}(\tau)$ as a function of τ we use the function:

$$g_{4-level}^{(2)}(\tau) = 1 - (1 + a_1 + a_2)e^{-\tau/\tau_1} + a_1e^{-\tau/\tau_2} + a_2e^{-\tau/\tau_3} \quad (49)$$

where $\lambda_i = 1/\tau_i$, $i \in \{1, 2, 3\}$ are the measured thermalization rates for the 2 NV system. We refer to the Eqs. 42 and 46. We observe that 8 exponents should be visible for 2 NV centers which are not interacting and 4 exponents for 2 interacting NV centers. We find that the fitting function is closest to that of 2 NV centers interacting via dipole-dipole interaction. Further, the fourth exponent is not visible in the measured data probably because the time constant is smaller than that of the instrument (see Supplementary Information for details). From the fit, we obtain three lifetimes corresponding to three energy levels above the ground state. We comment on the extracted lifetimes further in this section.

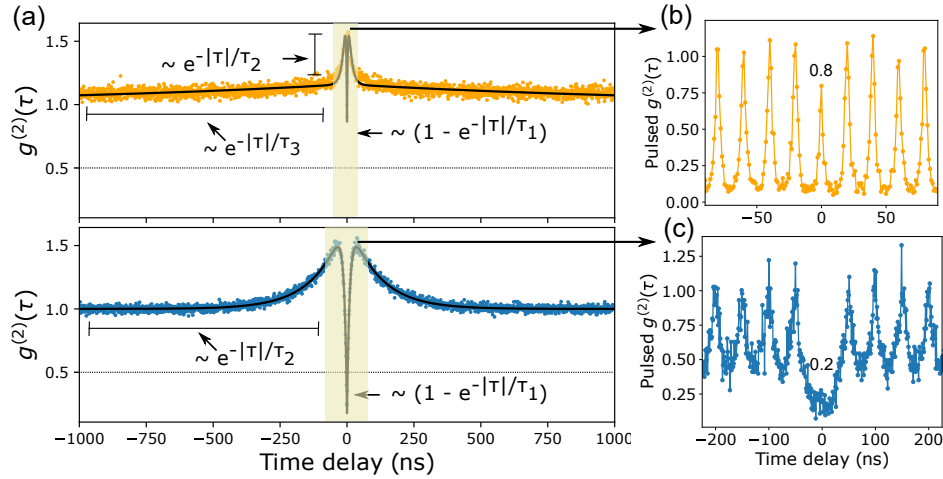


FIG. 3. **Evidence of a four-level energy structure:** (a) Expanded view of the cw $g^{(2)}(\tau)$ (measured: dots; fitting: solid line) for P_4 and P_1 highlighting the regions showing three exponential (top panel) and two exponential (bottom panel) decays, respectively. Two and three time constants in $g^{(2)}(\tau)$ correspond to a three and four energy level structure. The dashed line indicates $g^{(2)}(0) = 0.5$. For antibunching $g^{(2)}(0) < 0.5$, which is the case for P_1 , whereas $g^{(2)}(0) > 0.5$. (b)-(c) Pulsed $g^{(2)}(\tau)$ measurements (pump is pulsed at 50 MHz and 20 MHz, respectively, with ~ 200 ps pulses) are performed for the shaded yellow region of the cw $g^{(2)}(\tau)$ from P_4 and P_1 . The functional form of $g^{(2)}(\tau)$ and loss of antibunching $g^{(2)}(0) > 0.5$ indicate a coupling of two emitters in P_4 .

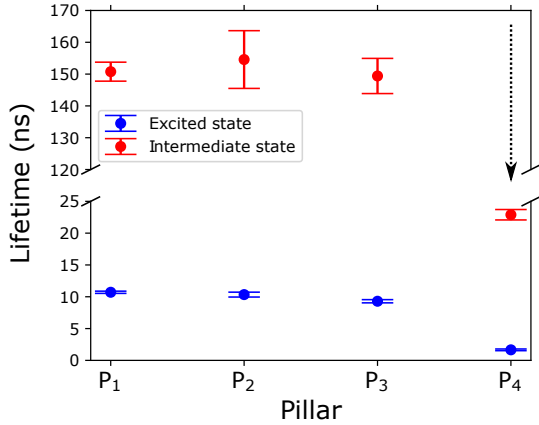


FIG. 4. **Interaction between two emitters:** Extracted (from $g^{(2)}(\tau)$) lifetimes of excited and metastable states (one of the intermediate states for P_4) are shown in blue and red dots with error bars. The dashed arrow indicates the lifetimes for P_4 which is reduced by a factor of ~ 6 than the other emitters (and also from the reported values), indicating an interaction between two emitters.

3. Comparison of Emission Properties for various pillars

We portray the difference in the $g^{(2)}(\tau)$ functions for two of the pillars P_1 and P_4 in Fig. 3 (a). We observe that for P_4 , the function shows three exponential components whereas for P_1 there are only two. We perform pulsed second-order correlation function measurement for the shaded region of Fig. 3 (a), for both P_4 and P_1 shown in Figs. 3 (b) and (c), respectively. The peak at $\tau = 0$

represents the probability of an emission pulse containing more than one photon. The measurement is conducted at 50 and 20 MHz repetition rates for P_4 and P_1 , yielding $g^{(2)}(0) = 0.8$ and 0.23, respectively.

In Fig. 4, we show the lifetimes of two energy levels for the various pillars. For P_1, \dots, P_3 , the excited and intermediate state lifetimes are ≈ 11 ns and ≈ 150 ns, close to the reported values for NV centers. However, for P_4 [shown with dashed arrow], we observe that the excited and one of the intermediate state lifetimes reduce to ≈ 2 ns and ≈ 23 ns, respectively. The observations of $0.5 < g^{(2)}(0) < 1$, measured $g^{(2)}(\tau)$ indicating a four energy-level scheme and reduction in the lifetimes all point towards the fact that the pillar P_4 contains two coupled emitters.

B. Decay Constants of the Energy Levels

Through the second-order correlation function, one can determine the individual decay rates involved in the system to gain a better understanding of the energy-level structure. For this purpose, we measure the second-order correlation function various pillars containing NV centers as a function of excitation power with the HBT interferometer. For brevity and comparison of single and two emitter systems, the $g^{(2)}(\tau)$ function and the extracted lifetimes for P_1 and P_4 as a function of power are shown in Figs. 5 (a)-(d). The $g^{(2)}(\tau)$ functions as a function of power for the pillars P_2, P_3 are shown in the Supplementary information. The measured and fitted $g^{(2)}(\tau)$ curves for some of the powers for the single emitter (P_1) and two-emitter (P_4) systems are shown in Fig. 5 (a) -

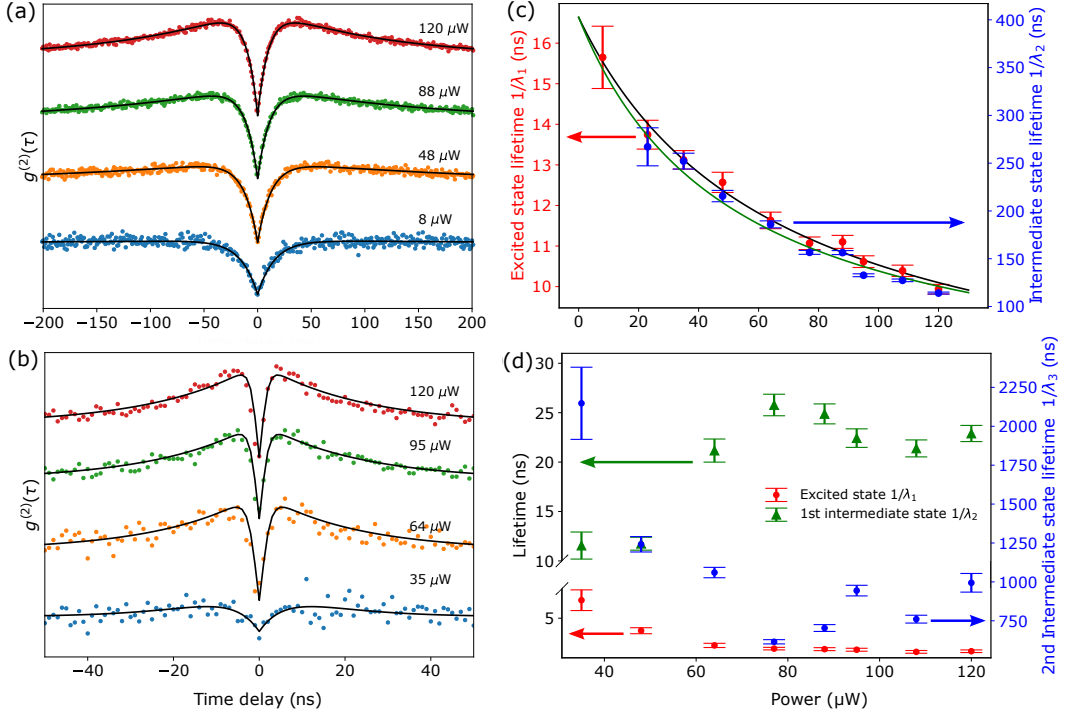


FIG. 5. **Time constants of the energy levels with pump power:** Measured $g^{(2)}(\tau)$ functions at various pump powers are shown for (a) P_4 and (b) P_1 [measured: dots; fitting: solid line]. The extracted lifetimes for (c) P_4 : excited state (blue dots), first intermediate state (green triangles) and second intermediate state (red dots - right axis), and (d) P_1 : excited state (red dots) and metastable (intermediate) state (blue dots). For P_1 , the solid lines show the fittings of the lifetimes (with Eqs. 34 and 35) as a function of pump power, revealing the spontaneous emission rate at the zero optical power limit.

(b), respectively. It can be seen as the power increases, there is an increase in the amplitude of the bunched behaviour, arising due to the shelving of the emitter in the metastable state [46, 47].

The intensity correlation functions for P_1 and P_4 at various powers were fit using Eqs. 48 and 49, respectively. The characteristic time scales (inverse of decay rates: $1/\lambda_1$ and $1/\lambda_2$) are plotted with excitation power for P_1 and P_4 in Fig. 5 (c) and (d), respectively. For P_1 the expected hyperbolic behaviour of $1/\lambda_i$ ($i \in \{1, 2\}$) is observed as a function of power, which we recover from Eqs. 34 - 35 where pump power described by r_{ge} [see Fig. 5 (c)]. In the limit of zero pump power, the spontaneous emission lifetimes are recovered (from fitting Eqs. 34 - 35), as ≈ 16 ns (excited state) and ≈ 400 ns (metastable state) for P_1 , as expected for single NV centers [48].

For P_4 , the excited state and one of the metastable states follow a hyperbolic trend with the excitation power, however the other metastable state approaches a saturated value [see Fig. 5 (d)].

From Eqs. 34 - 35, $1/\lambda_1$ for a 3-level system can be written as:

$$\tau_1 = \frac{1}{\lambda_1} = \frac{1}{r_{ge} + r_{eg}} \quad (50)$$

And for $1/\lambda_2$:

$$\tau_2 = \frac{1}{\lambda_2} = \frac{1}{r_{ei} + r_{ig}r_{eg}/\lambda_1} \quad (51)$$

Since the transition rate r_{eg} describes the transition from the ground to the excited state, it is related to the excitation power. Thus, the fittings in Eq. 5 (c) show the expected trend (governed by Eqs. 50- 51) thus ensuring the correct behaviour for P_1 (containing single NV).

In Fig. 5 (d), we see the behaviour of the inverse of the decay rates ($1/\lambda_i$ ($i \in \{1, 2, 3\}$)) for P_4 . It can be seen that $1/\lambda_{1,2}$ follows a hyperbolic behaviour. However, $1/\lambda_3$ shows the inverse behaviour, i.e., reaching a saturation.

C. Quantum Random Number Generation

To study one application of two-emitter systems, we discuss the possibility of quantum random number generation from these sources. We discuss a random binary sequence generator, where the bits 0 and 1 are assigned to clicks on the detectors A and B, respectively at the output modes of a symmetric beam-splitter. The emitted PL from each of $\{P_1, \dots, P_4\}$ is inputted to one input mode of a beam-splitter and the other input arm is blocked (describing the vacuum state $|0\rangle$). Each photon

in the stream of photons of the emission will randomly get transmitted or reflected based on the splitting ratio of the beam-splitter. Thus, the inherent quantumness of the "which-path" concept is used as the principle for random number generation.

1. Statistical Tests for Determining Randomness

We record time-tagged photon arrivals across two single-photon detectors (SPD) to obtain a random binary sequence. Clicks in one SPD are recorded as 0 and the other is recorded as 1. The sequence of raw random bits is post-processed using von Neumann's de-biasing procedure, to extract unbiased random numbers for our study. Using this, we eliminate some co-dependence of two adjacent bits. For every pair of generated bits, 00 and 11 are discarded, and 01 and 10 are replaced by 0 and 1, respectively. We perform this debiasing protocol in real time in our data acquisition program.

We collect and analyze the data for the pillars of interest P_1, \dots, P_4 . We obtain a generation rate of 540 kHz, 325 kHz, 760 kHz, and 170 kHz from pillars P_1, P_2, P_3 and P_4 , respectively, as we restrict to lower excitation powers (discussed in Sec. III C 2). The unbiased sequences are tested using a Python implementation of the NIST Statistical Test Suite, which is generally used to evaluate a binary sequence's randomness. The passing of each subtest is determined by the p value where $p = 1 - \alpha$, α is the significance level set to 0.01 by the test suite. Given $\alpha = 0.01$, $p > 0.01$ for a sequence to be considered random by a subtest.

As shown in Fig. 6, the random number sequences generated for pillars P_1, P_2, P_3 fail the runs test whereas that for P_4 passes all the subtests with $p > 0.01$. The Runs test determines whether uninterrupted sequences of identical bits occur as expected for an ideal random sequence of the same length as the measured sequence. We have observed that on repeated trials of data acquisition from the emitters, P_4 consistently show randomness by passing all the NIST subtests. In contrast, the other emitters often fail the Runs test. One can remedy this by performing an in-place shuffling of the sequence which is similar to a pseudo-random protocol on the extracted true random number sequence. Interestingly, P_4 passes all the subtests for every run proving to be a reliable source of quantum random numbers. The measure of randomness of the emitters is subject to its intrinsic properties and non-idealities of an experimental setup, which is considered further on.

2. Entropy of the source \mathcal{E} non-idealities of detection

The probability of whether a photon is linked to the reflectivity (R) and transmittivity (T) of the beam-splitter. Assuming a loss-less beam-splitter ($T + R = 1$) does not guarantee an unbiased beam-splitter, where $R = T$. If

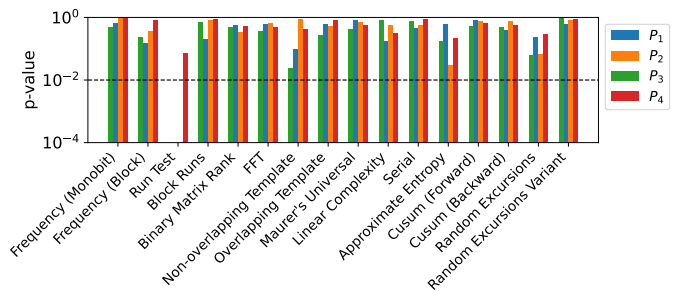


FIG. 6. **Comparison of quantum random number generation:** NIST test results for the random bit sequences generated from P_1, \dots, P_4 . The bits generated from P_4 pass all the tests with p -values > 0.01 with a higher proportion, indicating stronger reliability of randomness from such two coupled emitter systems.

$R \neq T$, it can produce some imbalance in the probabilities of the bits generated but does not introduce any memory in the system. Another parameter to be considered is the detection efficiencies (η_A, η_B) of the detectors used, which is a measure of the fraction of incident photons converted to detectable electrical signals. Finally, the dead times of the detectors (τ^A, τ^B), i.e., the time during which a consecutive detection event is suppressed, should be considered. It acts as a correction factor which relates the count rate to the actual photon flux onto the detector. For low incoming photon count rates and dark counts, this factor is close to unity. Thus, we restrict our measurements to low excitation power and comparatively low count rates. The dead times account for the undetected photon events by the detectors.

To quantify the randomness of the sources, we calculate the extractable entropy for the generators. The raw input bits collected from the single-photon detectors are post-processed since the true amount of randomness can be determined up to some accuracy. This is done by using the von Neumann debiasing protocol. Now, we must estimate the conditional min-entropy (H_∞) for the random sequence using:

$$H_\infty(X|Y) = -\log_2 \left(\sum_y p(y) \max\{p(x|y)\} \right) \quad (52)$$

where X, Y are two events, x, y are the subsequent random bits and $p(y), p(x|y)$ are the probabilities for occurrence of y and conditional occurrence of y if x occurs. For our case, $\{X, Y\} \in \{0, 1\}$, thus Eq. 52 can be written as:

$$H_\infty(X|Y) = -\log_2 \left(p(0) \max\{p(0|0), p(1|0)\} + p(1) \max\{p(0|1), p(1|1)\} \right) \quad (53)$$

Let us consider that the detector in the transmitted arm is A and that in the reflected arm is B. Therefore, the probability of the detector A (bit 1) or detector B (bit

0) clicking is given by $p(A)(\equiv p(0))$ or $p(B)(\equiv p(1))$, respectively. Similarly, the probability of detecting a subsequent photon in detector A[B] when it has already clicked a previous photon event is $p(A|A)[p(B|B)]$. The condi-

tional probabilities $p(A|A)$ and $p(B|A)$ are given as:

$$p(0|0) \equiv p(A|A) = \eta_A T \left(1 - \int_0^{\tau^A} g^{(2)}(\tau) d\tau \right) \quad (54)$$

$$p(1|0) \equiv p(B|A) = \eta_B R \left(1 - \eta_B R \left(\int_0^{\tau^B/2} g^{(2)}(\tau) d\tau \right)^2 \right) \quad (55)$$

where $\int_0^{\tau^A} g^{(2)}(\tau) d\tau$ signifies the probability that the next incident photon is in the dead time of detector A. The second term in Eq. 55 signifies the probability of detector B not being in its dead time when a photon shoots into the beam-splitter, this probability is an estimation, which is based on the assumption both dead times are approximately equal.

The probability ($p(A) \equiv p(0)$) of detector A detecting a photon is:

$$p(A) = \frac{r_A}{r_{\text{total}}} = \frac{r_A}{r_A + r_B}, \quad (56)$$

$$r_A = \eta_A T - \frac{(\eta_A T)^2 I_{\text{in}} \int_0^{\tau^A} g^{(2)}(\tau) d\tau}{4} \quad (57)$$

$$r_B = \eta_B R - \frac{(\eta_B R)^2 I_{\text{in}} \int_0^{\tau^B} g^{(2)}(\tau) d\tau}{4} \quad (58)$$

where r_A and r_B are the click rates of detector A and B and I_{in} is the incoming intensity impinging on the beam-splitter.

$p(AB)$. Thus, the above equation can be modified to:

$$H_{\infty}(X|Y) = -\log_2 \left(\max\{p(A) - p(AB), p(AB)\} + \max\{p(AB), 1 - p(A) - p(AB)\} \right) \quad (59)$$

Now, we introduce $p(AB) = p(A)p(B|A)$ and $p(BA) =$

Under the following conditions, $H_{\infty}(X|Y)$ yields the following results:

$$H_{\infty}(X|Y) = \begin{cases} -\log_2(p(A)) & p(A) - p(AB) \geq p(AB) \text{ and } p(AB) \geq 1 - p(A) - p(AB), \\ -\log_2(p(B)) & p(A) - p(AB) \leq p(AB) \text{ and } p(AB) \leq 1 - p(A) - p(AB), \\ -\log_2(2p(AB)) & p(A) - p(AB) \leq p(AB) \text{ and } p(AB) \geq 1 - p(A) - p(AB), \\ -\log_2(1 - 2p(A)) & p(A) - p(AB) \geq p(AB) \text{ and } p(AB) \leq 1 - p(A) - p(AB) \end{cases} \quad (60)$$

Since all four conditions have only one variable, we must have:

$$H_{\infty}(X|Y) = -\log_2(\max\{p(A), 1 - p(A), 2p(AB), 1 - 2p(AB)\}) \quad (61)$$

Using the parameters for our detectors: $\eta_A = 40\%$, $\tau^A = 77.9$ ns, $\tau^B = 74.7$ ns and

beam-splitter: $R = 0.55, T = 0.45$ we obtain, $p(A) = \{0.6097, 0.6098, 0.6095, 0.7098\}$ for emitters $\{P_1, P_2, P_3, P_4\}$, respectively. Further, $p(A)$ is the maximum value for function $\{p(A), 1 - p(A), 2p(AB), 1 - 2p(AB)\}$. Thus, for the pillars $\{P_1, P_2, P_3, P_4\}$, we extract $H_{\infty}(X|Y) = \{0.75126, 0.75129, 0.751201, 0.77081\}$, respectively with $H_{\infty}(X|Y) > 0 \forall$ emitters and

$H_\infty(X|Y)$ being maximum for P_4 . Since conditional min-entropy acts as a metric for randomness, we can conclude that all pillars generate random sequences with P_4 having a higher randomness per quantum bit.

3. Check for Background Noise

To comment on the emission properties from P_4 , we consider the probability of detecting an uncorrelated background noise event. The background emission from the sample's local environment, laser leakage, dark counts and electrical jitter can all be considered as background contributions leading to an increase in the value of $g^{(2)}(0)$. Since these spurious, uncorrelated events remain in the final raw bit sequence, we now understand their contribution to the conditional min-entropy $H_\infty(X|Y)$.

We introduce the parameter p_e , representing the probability of detecting a background noise event. The conditional min-entropy thus modifies to:

$$H_\infty(X|Y) = -\log_2 \left(p_e + (1 - p_e)f(p) \right) \quad (62)$$

where $f(p) = \max\{p(A), 1 - p(A), 2p(AB), 1 - 2p(AB)\}$ where $p_e = 1 - \sqrt{1 - g^{(2)}(0)}$. since the fraction of single photon events is $\sqrt{1 - g^{(2)}(0)}$. Here we assume that for P_4 $g^{(2)}(0) > 0.5$ is caused due to increased background (spurious) noise events. For P_4 , $g^{(2)}(0) \approx 0.8$ and $p_e = 0.2$, i.e., $H_\infty(X|Y) \rightarrow 0.1$, which is small compared to the other pillars. Therefore, if the increase in $g^{(2)}(0)$ is due to background events, randomness per quantum bit should decrease, contradictory to our experimental observations. For two emitters, all the events are from single

photon sources, thereby of a source of randomness. This is why emission from P_4 can generate random sequences.

Thus, as the two-emitter system shows a higher passing proportion for the NIST subtests and the largest conditional min-entropy compared to the single emitters, we conclude that it can act as a reliable source of random numbers.

IV. CONCLUSION

We experimentally show the superradiant behaviour from two NV centers in a diamond nanopillar. We observe a $g^{(2)}(0) > 0.5 \rightarrow 1$ and drastic reductions in the lifetimes of the excited and intermediate states of the system, which are considered the signature of cooperative effects from a system of emitters. We also show the effect of excitation power on the lifetimes of the various energy levels of the emitters for a system of two emitters and a single emitter. We solve the Lindblad master equation for light interacting with a single emitter, two emitters with and without dipole-dipole coupling at finite temperature, in the superradiant regime, and derive the second-order correlation function from the jump operators used to describe the Lindbladian. In the process, we also discover that for the two emitter cases, the populations and coherence do not mix. Our theoretical analysis for a system of NV centers interacting with an environment consisting of the excitation pump and a phonon bath (also taking into account that the experiment was conducted at room temperature), supports our experimental results. Finally, we show an application of our system of emitters in the context of random number generation. The two-emitter system showing superradiant behaviour can produce reliable random number sequences with a generation rate of ~ 200 kHz at low pump powers.

-
- [1] K. Takemoto, Y. Nambu, T. Miyazawa, Y. Sakuma, T. Yamamoto, S. Yorozu, and Y. Arakawa, *Sci. Rep.* **5**, 14383 (2015).
 - [2] Q. Luo, Z. Cheng, J. Fan, L. Tan, H. Song, G. Deng, Y. Wang, and Q. Zhou, *Optics Letters* **45**, 4224 (2020).
 - [3] J. E. Gentle, W. K. Härdle, and Y. Mori, (2012).
 - [4] W. Tittel, H. Zbinden, and N. Gisin, *Physical Review A* **63**, 042301 (2001).
 - [5] M. Giustina, M. A. Versteegh, S. Wengerowsky, J. Handsteiner, A. Hochrainer, K. Phelan, F. Steinlechner, J. Kofler, J.-Å. Larsson, C. Abellán, *et al.*, *Physical review letters* **115**, 250401 (2015).
 - [6] M. Applegate, O. Thomas, J. Dynes, Z. Yuan, D. Ritchie, and A. Shields, *Applied Physics Letters* **107** (2015).
 - [7] M. A. Wayne, E. R. Jeffrey, G. M. Akselrod, and P. G. Kwiat, *Journal of Modern Optics* **56**, 516 (2009).
 - [8] C. Gabriel, C. Wittmann, D. Sych, R. Dong, W. Mauerer, U. L. Andersen, C. Marquardt, and G. Leuchs, *Nature Photonics* **4**, 711 (2010).
 - [9] Z. Yuan, M. Lucamarini, J. Dynes, B. Fröhlich, A. Plews, and A. Shields, *Applied Physics Letters* **104** (2014).
 - [10] H. Guo, W. Tang, Y. Liu, and W. Wei, *Physical Review E* **81**, 051137 (2010).
 - [11] Y. Liu, Q. Zhao, M.-H. Li, J.-Y. Guan, Y. Zhang, B. Bai, W. Zhang, W.-Z. Liu, C. Wu, X. Yuan, *et al.*, *Nature* **562**, 548 (2018).
 - [12] M. Herrero-Collantes and J. C. Garcia-Escartin, *Reviews of Modern Physics* **89**, 015004 (2017).
 - [13] S. J. White, F. Klauck, T. T. Tran, N. Schmitt, M. Kianinia, A. Steinfurth, M. Heinrich, M. Toth, A. Szameit, I. Aharonovich, *et al.*, *Journal of Optics* **23**, 01LT01 (2020).
 - [14] X. Chen, J. N. Greiner, J. Wrachtrup, and I. Gerhardt, *Scientific reports* **9**, 18474 (2019).
 - [15] L. Oberreiter and I. Gerhardt, *Laser & Photonics Reviews* **10**, 108 (2016).
 - [16] Y. Jian, M. Ren, E. Wu, G. Wu, and H. Zeng, *Review of Scientific Instruments* **82** (2011).

- [17] S. Strauf, N. G. Stoltz, M. T. Rakher, L. A. Coldren, P. M. Petroff, and D. Bouwmeester, *Nat. Photonics* **1**, 704 (2007).
- [18] C. Santori, M. Pelton, G. Solomon, Y. Dale, and Y. Yamamoto, *Phys. Rev. Lett.* **86**, 1502 (2001).
- [19] B. Lounis and W. E. Moerner, *Nature* **407**, 491 (2000).
- [20] M. G. Dastidar, I. Thekkooden, P. K. Nayak, and V. P. Bhallamudi, *Nanoscale* **14**, 5289 (2022).
- [21] I. Aharonovich, D. Englund, and M. Toth, *Nat. Photonics* **10**, 631 (2016).
- [22] C. Kurtsiefer, S. Mayer, P. Zarda, and H. Weinfurter, *Phys. Rev. Lett.* **85**, 290 (2000).
- [23] T. Plakhotnik and H. Aman, *Diam. Relat. Mater.* **82**, 87 (2018).
- [24] Y. Yonezu, K. Wakui, K. Furusawa, M. Takeoka, K. Semba, and T. Aoki, *Sci. Rep.* **7**, 12985 (2017).
- [25] G. Balasubramanian, P. Neumann, D. Twitchen, M. Markham, R. Kolesov, N. Mizuochi, J. Isoya, J. Achard, J. Beck, J. Tessler, *et al.*, *Nat. Mater.* **8**, 383 (2009).
- [26] T. Gaebel, M. Domhan, I. Popa, C. Wittmann, P. Neumann, F. Jelezko, J. R. Rabreau, N. Stavrias, A. D. Greentree, S. Praver, *et al.*, *Nat. Phys.* **2**, 408 (2006).
- [27] E. Petkov, T. Rendler, C. Petkov, F. Schnabel, J. Reithmaier, J. Wrachtrup, C. Popov, and W. Kulisch, *Phys. Status Solidi A* **210**, 2066 (2013).
- [28] S. A. Momenzadeh, R. J. Stohr, F. F. De Oliveira, A. Brunner, A. Denisenko, S. Yang, F. Reinhard, and J. Wrachtrup, *Nano Lett.* **15**, 165 (2015).
- [29] S. Hong, M. S. Grinolds, L. M. Pham, D. Le Sage, L. Luan, R. L. Walsworth, and A. Yacoby, *MRS Bull.* **38**, 155 (2013).
- [30] J. Riedrich-Möller, L. Kipfstuhl, C. Hepp, E. Neu, C. Pauly, F. Mücklich, A. Baur, M. Wandt, S. Wolff, M. Fischer, *et al.*, *Nat. Nanotechnol.* **7**, 69 (2012).
- [31] A. Faraon, C. Santori, Z. Huang, V. M. Acosta, and R. G. Beausoleil, *Phys. Rev. Lett.* **109**, 033604 (2012).
- [32] B. Khanaliloo, M. Mitchell, A. C. Hryciw, and P. E. Barclay, *Nano Lett.* **15**, 5131 (2015).
- [33] E. M. Purcell, in *Confined Electrons and Photons: New Physics and Applications* (Springer, 1995) pp. 839–839.
- [34] H. Paul, *Rev. Mod. Phys.* **54**, 1061 (1982).
- [35] S. Kitson, P. Jonsson, J. Rarity, and P. Tapster, *Phys. Rev. A* **58**, 620 (1998).
- [36] S. Li, W. Li, V. V. Yakovlev, A. Kealy, and A. D. Greentree, *Optics Express* **30**, 12495 (2022).
- [37] J. G. Worboys, D. W. Drumm, and A. D. Greentree, *Physical Review A* **101**, 013810 (2020).
- [38] C. C. Gerry and P. L. Knight, *Introductory quantum optics* (Cambridge university press, 2023).
- [39] R. H. Dicke, *Physical review* **93**, 99 (1954).
- [40] C. Bradac, M. T. Johnsson, M. v. Breugel, B. Q. Baragiola, R. Martin, M. L. Juan, G. K. Brennen, and T. Volz, *Nature communications* **8**, 1205 (2017).
- [41] J. Maze Ríos, (2011).
- [42] H.-P. Breuer and F. Petruccione, *The theory of open quantum systems* (OUP Oxford, 2002).
- [43] M. Cygorek, E. D. Scerri, T. S. Santana, Z. X. Koong, B. D. Gerardot, and E. M. Gauger, *Physical Review A* **107**, 023718 (2023).
- [44] Y.-D. Qu, Y. Zhang, P. Ni, C. Shan, H. David, and K. Mølmer, arXiv preprint arXiv:2407.09755 (2024).
- [45] S. Schietinger, M. Barth, T. Aichele, and O. Benson, *Nano letters* **9**, 1694 (2009).
- [46] F. Treussart, A. Clouqueur, C. Grossman, and J.-F. Roch, *Optics Letters* **26**, 1504 (2001).
- [47] I. Aharonovich, S. Castelletto, D. Simpson, A. Greentree, and S. Praver, *Physical Review A* **81**, 043813 (2010).
- [48] J. Storteboom, P. Dolan, S. Castelletto, X. Li, and M. Gu, *Opt. Express* **23**, 11327 (2015).

Appendix A: Bath in thermal state

Let $\rho_B = \prod_{k,\lambda} (1 - e^{-\beta\hbar\omega_k}) e^{-\beta\hbar\omega_k} b_\lambda^\dagger b_\lambda$ and $N(\omega_k) = \frac{1}{e^{\beta\hbar\omega_k} - 1}$. Using the above expression for \vec{E} in Eq. 21 we have:

$$\begin{aligned} \gamma_{ij}(\omega) = \sum_{k,k'} \sum_{\lambda,\lambda'} \sqrt{\frac{2\pi\omega_k}{V}} \sqrt{\frac{2\pi\omega_{k'}}{V}} \vec{d}^* \cdot \vec{e}_\lambda(\vec{k}) \vec{d} \cdot \vec{e}_{\lambda'}(\vec{k}') \int_0^\infty dt e^{i\omega t} \left[\langle b_\lambda(\vec{k}) b_{\lambda'}(\vec{k}') \rangle e^{i\vec{k} \cdot (\vec{r}_i + \vec{r}_j)} e^{-i\omega_k t} - \langle b_\lambda^\dagger(\vec{k}) b_{\lambda'}(\vec{k}') \rangle e^{-i\vec{k} \cdot (\vec{r}_i - \vec{r}_j)} e^{i\omega_k t} \right. \\ \left. - \langle b_\lambda(\vec{k}) b_{\lambda'}^\dagger(\vec{k}') \rangle e^{i\vec{k} \cdot (\vec{r}_i - \vec{r}_j)} e^{-i\omega_k t} + \langle b_\lambda^\dagger(\vec{k}) b_{\lambda'}^\dagger(\vec{k}') \rangle e^{-i\vec{k} \cdot (\vec{r}_i + \vec{r}_j)} e^{i\omega_k t} \right] \end{aligned} \quad (\text{A1})$$

where,

$$\langle b_\lambda(\vec{k}) b_{\lambda'}(\vec{k}') \rangle = \langle b_\lambda^\dagger(\vec{k}) b_{\lambda'}^\dagger(\vec{k}') \rangle = 0 \quad (\text{A2})$$

$$\langle b_\lambda^\dagger(\vec{k}) b_{\lambda'}(\vec{k}') \rangle = \delta_{kk'} \delta_{\lambda\lambda'} N(\omega) \quad (\text{A3})$$

$$\langle b_\lambda(\vec{k}) b_{\lambda'}^\dagger(\vec{k}') \rangle = \delta_{kk'} \delta_{\lambda\lambda'} (1 + N(\omega)) \quad (\text{A4})$$

Using this in Eq. A1 we get:

$$\gamma_{ij}(\omega) = - \sum_{k,\lambda} \frac{2\pi\omega_k}{V} \vec{d}^* \cdot \vec{e}_\lambda(\vec{k}) \vec{d} \cdot \vec{e}_\lambda(\vec{k}) \int_0^\infty dt \left[N(\omega) e^{-i\vec{k} \cdot (\vec{r}_i - \vec{r}_j)} e^{i(\omega_k + \omega)t} + (1 + N(\omega)) e^{i\vec{k} \cdot (\vec{r}_i - \vec{r}_j)} e^{-i(\omega_k - \omega)t} \right] \quad (\text{A5})$$

In the continuum limit of radiation modes, we have:

$$\frac{1}{V} \sum_k \rightarrow \int \frac{d^3k}{(2\pi)^3} = \frac{1}{(2\pi)^3} \int k^2 dk \int d\Omega = \frac{1}{(2\pi)^3} \int (\omega_k/c)^2 d(\omega_k/c) \int d\Omega = \frac{1}{(2\pi c)^3} \int_0^\infty d\omega_k \omega_k^2 \int d\Omega \quad (\text{A6})$$

With this and using $e^{l_\lambda(\vec{k})} e^{m_\lambda(\vec{k})} = \delta_{lm} - \frac{k_l k_m}{|\vec{k}|^2}$, we write:

$$\begin{aligned} \sum_{k,\lambda} \frac{2\pi\omega_k}{V} \vec{d}^* \cdot \vec{e}_\lambda(\vec{k}) \vec{d} \cdot \vec{e}_\lambda(\vec{k}) e^{i\vec{k} \cdot (\vec{r}_i - \vec{r}_j)} &= \frac{1}{(2\pi)^2 c^3} \int d\Omega \left(\vec{d}^* \cdot \vec{d} - \frac{(\vec{k} \cdot \vec{d}^*)(\vec{k} \cdot \vec{d})}{k^2} \right) e^{i\vec{k} \cdot (\vec{r}_i - \vec{r}_j)} = \frac{4}{(2\pi)^2 c^3} d^2 (j_0(x_{ij}) + P_2(\cos \theta_{ij}) j_2(x_{ij})) \\ &= \sum_{k,\lambda} \frac{2\pi\omega_k}{V} \vec{d}^* \cdot \vec{e}_\lambda(\vec{k}) \vec{d} \cdot \vec{e}_{\lambda'}(\vec{k}') e^{-i\vec{k} \cdot (\vec{r}_i - \vec{r}_j)} \end{aligned} \quad (\text{A7})$$

where $j_0(x) = \frac{\sin x}{x}$, $j_2(x) = (\frac{3}{x^3} - \frac{1}{x}) \sin x$ and $P_2(\cos \theta) = \frac{1}{2}(3 \cos^2 \theta - 1)$ where $x_{ij} = \frac{\omega_k}{c} |r_i - r_j|$ and $\cos \theta_{ij} = \frac{|\vec{d} \cdot (\vec{r}_i - \vec{r}_j)|^2}{d^2 |\vec{r}_i - \vec{r}_j|^2}$. Let $f(x_{ij}, \theta_{ij}) = j_0(x_{ij}) + P_2(\cos \theta_{ij}) j_2(x_{ij})$.

Using the above, $\int_0^\infty ds e^{-ixs} = \pi \delta(x) - iP \frac{1}{x}$ and $\int_0^\infty ds e^{ixs} = 3\pi \delta(x) - iP \frac{1}{x}$ where P is Cauchy principal value, in Eq. A5 we have:

$$\gamma_{ij}(\omega) = -\frac{2}{3\pi c^3} d^2 \left[\int_0^\infty d\omega_k \omega_k^3 f(x_{ij}, \theta_{ij}) \int_0^\infty dt \left((1 + N(\omega_k)) e^{-i(\omega - \omega_k)t} + N(\omega_k) e^{i(\omega + \omega_k)t} \right) \right] \quad (\text{A8})$$

$$\begin{aligned} &= -\frac{2}{3\pi c^3} d^2 \left[\pi \omega_k^3 f(x_{ij}, \theta_{ij}) [(1 + N(\omega_k)) \delta(\omega - \omega_k) + 3N(\omega_k) \delta(\omega + \omega_k)] \right. \\ &\quad \left. - iP \int_0^\infty d\omega_k \omega_k^3 f(x_{ij}, \theta_{ij}) \left(\frac{1 + N(\omega_k)}{\omega - \omega_k} + \frac{N(\omega_k)}{\omega + \omega_k} \right) \right] \end{aligned} \quad (\text{A9})$$

Using $N(-\omega) = -(1 + N(\omega))$ we have:

$$\gamma_{ij}(\omega) = d^2 \left[\frac{4\omega^3}{3c^3} f\left(\frac{\omega}{c} |r_i - r_j|, \theta_{ij}\right) (1 + N(\omega)) + iP \int_0^\infty d\omega_k \omega_k^3 f(x_{ij}, \theta_{ij}) \left(\frac{1 + N(\omega_k)}{\omega - \omega_k} + \frac{N(\omega_k)}{\omega + \omega_k} \right) \right] \quad (\text{A10})$$

Appendix B: Bath in Coherent State

The sample is excited using a single-mode, coherent laser having a fixed wavelength (λ_α), mode (k_α) and polarization (\vec{e}_{λ_α}) as the pump. Thus, we now consider $\rho_B = |\alpha\rangle\langle\alpha|_{k_\alpha, \lambda_\alpha}$. Then we write $b_{\lambda_\alpha}(k_\alpha) \equiv b_\alpha$:

$$\langle b_\alpha b_\alpha \rangle = \langle b_\alpha^\dagger b_\alpha^\dagger \rangle = 0 \quad (\text{B1})$$

$$\langle b_\alpha^\dagger b_\alpha \rangle = |\alpha|^2 \quad (\text{B2})$$

$$\langle b_\alpha b_\alpha^\dagger \rangle = (1 + |\alpha|^2) \quad (\text{B3})$$

We represent the pump laser used in the experiment as a single-mode electric field in a coherent state. For a single mode electromagnetic field propagating along the z direction, the electric field is given by $\vec{E}(\vec{r}_i) = \sqrt{\frac{2\pi\hbar\omega_\alpha}{L^3}} \vec{e}_{\lambda_\alpha} (b e^{i\vec{k}_\alpha \cdot \vec{z}_i} - b^\dagger e^{-i\vec{k}_\alpha \cdot \vec{z}_i})$. Here L is the cavity length through which the field propagates. Using the above for Eq. A1 we have:

$$\begin{aligned} \gamma_{ij}(\omega) &= \frac{2\pi\omega_\alpha}{L^3} (\vec{d}^* \cdot \vec{e}_{\lambda_\alpha}) (\vec{d} \cdot \vec{e}_{\lambda_\alpha}) \int_0^\infty dt \left[\langle b_\alpha^\dagger b_\alpha \rangle e^{-ik_\alpha \cdot (z_i - z_j)} e^{i(\omega_\alpha + \omega)t} + \langle b_\alpha b_\alpha^\dagger \rangle e^{ik_\alpha \cdot (z_i - z_j)} e^{-i(\omega_\alpha - \omega)t} \right] \\ &= \frac{2\pi\omega_\alpha}{L^3} (\vec{d}^* \cdot \vec{e}_{\lambda_\alpha}) (\vec{d} \cdot \vec{e}_{\lambda_\alpha}) \int_0^\infty dt \left[|\alpha|^2 e^{i(\omega_\alpha + \omega)t} + (1 + |\alpha|^2) e^{-i(\omega_\alpha - \omega)t} \right] \\ &= \frac{2\pi\omega_\alpha}{L^3} |d_\alpha|^2 \left[|\alpha|^2 \int_0^\infty dt e^{i(\omega_\alpha + \omega)t} + (1 + |\alpha|^2) \int_0^\infty dt e^{-i(\omega_\alpha - \omega)t} \right] \end{aligned} \quad (\text{B4})$$

where we have used $z_i - z_j = 0$ as all emitters are in the same plane and $|d_\alpha|^2$ is the dipole moment along the axis of polarization of $|\alpha\rangle\langle\alpha|$. Now using the relations $\int_0^\infty ds e^{-ixs} = \pi\delta(x) - iP\frac{1}{x}$ and $\int_0^\infty ds e^{ixs} = 3\pi\delta(x) - iP\frac{1}{x}$, we have in Eq. B4:

$$\begin{aligned}\gamma_{ij}(\omega) &= \frac{2\pi\omega_\alpha}{L^3} |d_\alpha|^2 \left[|\alpha|^2 (3\pi\delta(\omega_\alpha + \omega) - iP\frac{1}{\omega_\alpha + \omega}) + (1 + |\alpha|^2) (\pi\delta(\omega_\alpha - \omega) - iP\frac{1}{\omega_\alpha - \omega}) \right] \\ &= \frac{2\pi^2\omega |d_\alpha|^2}{L^3} (1 - 2|\alpha|^2) - i\frac{2\pi\omega_\alpha}{L^3} |d_\alpha|^2 \left(|\alpha|^2 P\frac{1}{\omega_\alpha + \omega} + (1 + |\alpha|^2) P\frac{1}{\omega_\alpha - \omega} \right)\end{aligned}\tag{B5}$$
